# Photoluminescence and Hydrogen Gas-Sensing Properties of Titanium Dioxide Nanostructures Synthesized by Hydrothermal Treatments

Lucky M. Sikhwivhilu,* Siyasanga Mpelane, Bonex W. Mwakikunga,* and Suprakas Sinha Ray*

DST/CSIR Nanotechnology Innovation Centre, National Centre for Nano-Structured Materials, Council for Scientific and Industrial Research, Pretoria 0001, South Africa

ABSTRACT: Titanium dioxide (TiO_2) nanostructures were synthesized by microwave-assisted and conventionally heated hydrothermal treatment of TiO_2 powder. The tubular structures were converted to a rodlike shape by sintering the samples at various temperatures in air for 3 h. This was accompanied by phase transformation largely influenced by the method of synthesis and the mode of heating. The X-ray diffraction results are in agreement with the structural transformation indicating the gradual changes in the phase and crystallinity of the as prepared samples. The tubular structure is found to collapse at high temperature. UV−vis−IR spectroscopic results suggest that nanorods tend to absorb photons of higher energy ($\lambda = 280$ nm) than nanotubes ($\lambda = 300$ nm) but emit photons with lower energy than nanotubes. It was found that the nanotubes have a sharper photoluminance emission line at 340 nm that is absent in the nanorods. We also found that nanotubes have higher efficiency, lower threshold sensing temperature, longer response time, and shorter recovery time for hydrogen gas sensing than nanorods.

KEYWORDS: titanium dioxide nanostructures, synthesis and characterization, photoluminescence and hydrogen sensing behaviors
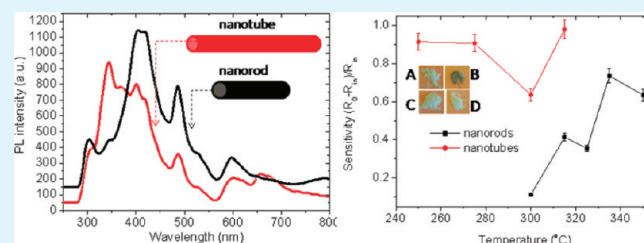
1. INTRODUCTION

One-dimensional TiO_2 derived materials such as nanowires,[1,2] nanoribbons,[3] nanotubes,[4] and nanorods[5] have attracted much attention because of their unique microstructure and properties.[6] Titanium dioxide derived nanotubes (TNT) are particularly interesting, partly because of their large specific surface area, which can potentially enhance the photocatalytic activity, leading to a higher potential of applications in environmental purification, decomposition of carbonic acid gas, and generation of hydrogen gas.[7−9] TiO_2 has superior physicochemical properties. Electrocatalysis, photocatalysis, hydrogen storage, and lithium batteries are among its applications. These have seen TiO_2-derived nanostructures become widely researched and explored materials for various applications.[10−13] TiO_2 has a wide variety of uses: from biocompatible materials to gas sensors, energy storage, photovoltaics, and photocatalysis. TiO_2 is one of the best-known photocatalytic materials. It is the model material in Gratzel's dye sensitized solar cells.[14] TiO_2 anatase has demonstrated the catalysis of photoactivated water splitting for the production of H_2 and O_2 gases. Although there has been intense debate on the feasibility of the TiO_2 water splitting, many authors confirm this interesting property,[15] which is a promising application toward the hydrogen economy.

Although there are various methods for the preparation of TiO_2 microstructures such as electrode reactions,[16] templating,[17−19] and replica process,[20] the alkali-based hydrothermal synthesis has become one of the most widely used technique to synthesize a range of TiO_2 derived 1D nanomaterials. The use of hydrothermal processing has been extended to produce other 1D TiO_2 nanostructures such as nanowires, nanofibers, etc., with different molecular structures depending on the synthesis conditions. Post-thermal treatment of these structures is known to lead to morphological and structural transformation. For example, tubular structures may transform to nanorodlike structure upon sintering. Although nanotubular structures are more desirable due to their high surface area, titanate nanotubes with free alkali ions are often unstable at high temperatures ($\sim$ 450 °C). To retain the 1D nanostructure at high temperatures ($\geq$450 °C), the solid nanowire or nanorod form is preferable.

Literature on optical properties of TiO_2 rarely discusses its photoluminescence (PL). The few reports available limit discussion only to a small visible band 300−500 nm.[21] Also the reported PL spectra are not well resolved and most authors ascribe these unresolved Lorentzian-shaped blackbody-like PL spectra of TiO_2 simply to surface-trapped excitons.

It is natural that since TiO_2 has been utilized in water splitting that TiO_2 can be employed as a hydrogen (H_2) gas sensor. Compared to the magnitude of research on TiO_2 properties in general, very few reports exist on TiO_2 as a hydrogen gas sensor.[22]

In this study, synthesis of TiO_2 derived nanotubes and nanorods by hydrothermal and thermal post-treatment,

respectively, will be reported. Furthermore, the effect of hydrothermal process using conventional heating and microwave irradiation on both the structure and phase composition is also reported herein. The extent of alkali ion intercalation into the structural framework of TiO_2 is assessed in relation to the method of heating. Consequently, how this will have an impact on the emission and absorption properties (luminescence and UV−vis) of the materials is tested. The PL spectra reported here are well resolved. Clear differences of PL and absorption properties depending on process of synthesis (the rapid microwave hydrothermal synthesis (μHS) versus the slow autoclaved hydrothermal synthesis (aHS)) and postsynthesis calcinations (nanotube versus nanorod) are shown. The H_2-sensing properties of TiO_2 in its nanotube and nanorod forms are reported and compared in this present work.

2. EXPERIMENTAL SECTION

2.1. Conventional Autoclave Heating Hydrothermal Synthesis (aHS) of TNT. About 22 g of P25 Degussa titania powder was placed in a 300 mL Teflon container together with 200 mL of KOH solution (18M). The mixture was stirred for 10 min on a magnetic stirrer to ensure homogeneous mixture. The mixture was then autoclave heated for 24 h at 150 °C with a constant stirring rate of 500 rpm. The solution was allowed to cool to room temperature and then washed with deionized water. This was followed by separation of solid product from the mixture by centrifugation. The washing process was repeated until the conductivity of the supernatant was less than 100 μS/cm. The solid product was oven-dried under vacuum at 120 °C for 14 h. The sample product was divided into four equal portions and then sintered for 3 h at 200, 400, 700, and 900 °C.

2.2. Microwave-Assisted Hydrothermal Synthesis (μHS) of TNT. The microwave assisted hydrothermal (HT) synthesis of TNT was analogous to the conventional heating HT process. However, for microwave assisted HT process the heating was done for only 15 min. In a typical procedure, 22 g of P25 Degussa titania powder and 200 mL of KOH (18M) solution were mixed in a 500 mL beaker. The mixture was stirred for 10 min on a magnetic stirrer. About 50 mL aliquots of the mixture were transferred into 4 Teflon vessels (100 mL each). The vessels were placed on a rotor and then into the microwave unit (Multiwave 3000 Microwave Reaction System). The mixture was processed for 15 min at the power output of 600 W. The product was allowed to cool and then washed with deionized water. The washing was done repeatedly until the conductivity was less than 100 μS/cm and then dried in a vacuum oven at 120 °C for 14 h. The sample product was divided into four equal portions and then sintered for 3 h at 200, 400, 700, and 900 °C.

2.3. Characterizations. X-ray diffraction measurements were carried out on a PANAnalytical X' Pert PRO PW 3040/60 X-ray diffractometer equipped with a Cu K$_\alpha$ wavelength of 0.154184 nm operating at 45 kV and 40 mA. The spectra were collected in reflection geometry at 2θ-values ranging from 10−80° with a step size of 0.02°. Raman measurements were made using the HR 800 micro-Raman attachment of a Jobin-Yvon T64000 Raman spectrometer, configured in triple subtractive mode. The excitation wavelength was 514.5 nm and the spectrometer was set at a spectral resolution of 0.4 cm^{-1}.

Nitrogen adsorption−desorption isotherms were measured on a Micromeritics TRISTAR II 3020 analyzer. Prior to analysis, samples were outgassed at 90 °C for a few hours under vacuum (200 mbar) and then at 120 °C for overnight under vacuum. The specific surface area of the nanostructures was determined by Brunauer−Emmett−Teller (BET) method.

High-resolution transmission electron microscope (TEM) images were obtained using a JEOL JSM 2100 TEM with a LaB$_6$-cathode operated at a voltage of 200 kV. High-resolution SEM measurements were made on ZEISS Auriga FIB-SEM operated at 2−5 keV.

The density of the powders produced was studied using a helium pycnometer (Acupyc 1340 Micromeritics apparatus). The apparatus was operated at room temperature.

Absorption spectra for the TiO_2 samples were obtained on Perkin-Elmer UV−vis−IR spectrophotometer at room temperature from 200−900 nm. Assessment of the photoluminescence of the samples was carried out using a NanoLog spectrometer at a detector temperature of liquid nitrogen with samples at room temperature and an excitation wavelength of 325 nm line of deuterium lamp. The emission was determined by a Jobin-Yvon photomultiplier tube detector.

H_2 sensing properties were obtained through a homemade gas sensing station at iThemba Laboratories in South Africa by measuring transient resistance of the samples when in dry air and also when a flow rate of 200 mL/min of H_2 gas was flown past the samples. Sensitivity, S (defined as $S = |R - R_{out}|/R_{out}$, where R and R_{out} are resistances after and before H_2 exposure, respectively) and response times, $\tau_{response}$, and recovery times, $\tau_{recovery}$, were calculated from the resistance versus time curves and are compared for nanotubes and nanorods in the later sections.

3. RESULTS AND DISCUSSION

3.1. Synthesis and Characterization of TiO_2 Nanostructures. Note that the conditions used for aHS and μHS for each method were optimized to give a 100% yield of tubular structures. Figures 1 (a) and (b) show the SEM images of
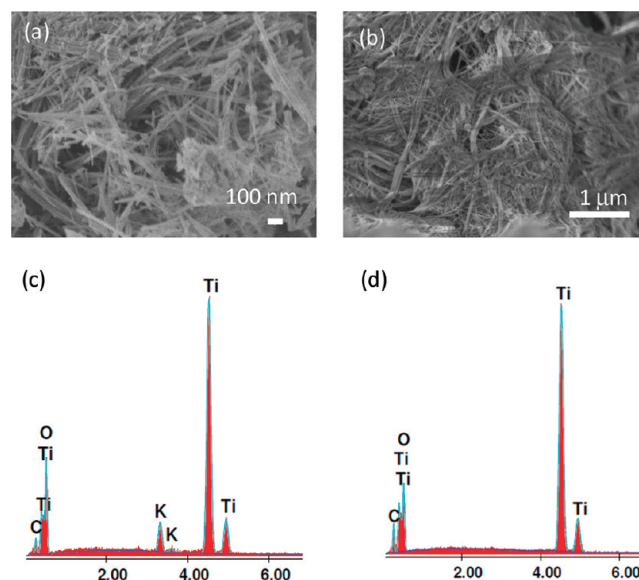

Figure 1. SEM images of (a) aHS1 and (b) μHS4 oven-dried at 120 °C for overnight. Typical energy dispersive spectra (EDS) of (c) the aHS samples and the μHS samples indicate presence and absence of potassium.

TNTs synthesized by hydrothermal (HT) processes using aHS (Figure 1a) and μHS (Figure 1b). Both samples were oven-dried at 120 °C for 14 h. After hydrothermally treating TiO_2 (P25 Degussa) in the presence of KOH in the autoclave a mixture of TNTs with smooth surface and rough surface (especially at ends) were obtained. μHS treated TNTs were found to have a relatively smoother surface. TNTs obtained by both methods exhibited similar size range (8−11 nm in diameter and lengths of a few hundred nanometers) and tended to agglomerate to form bundles. Both procedures generated TNTs that are open ended with the tube yields of close to 100%. μHS takes a few minutes, whereas aHS takes 24 h of processing.

Figure 2a shows the SEM images of sample prepared by aHS and μHS and sintered at various temperatures. The postsyn-
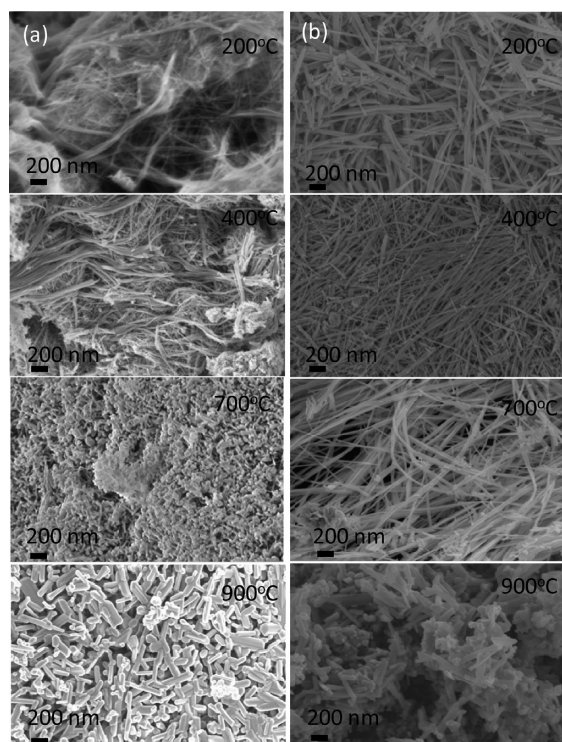
Figure 2. (a) SEM images of aHS-synthesized material sintered at different temperatures 200, 400, 700, and 900 °C. (b) SEM images of μHS -synthesized (15 min of processing) material sintered at different temperatures 200, 400, 700, and 900 °C.

thesis treatment was varied from 200 to 900 °C as shown in the micrographs. Postsynthesis treatment of aHS at 200 °C (Figure 2a) did not change the physical dimensions (diameter and length) and morphology when compared to the oven-dried sample. The sample remained tubular in shape with reasonably uniform size distribution (8−12 nm in diameter). Sintering at 400 °C (Figure 2b) led to the formation of bigger bundles (70−100 nm in diameter) and breaking of some tubes to form non one-dimensional materials. Individual tubes showed an average diameter of 14 nm suggesting particle growth. Elevating the temperature to 700 °C (Figure 2c) resulted in the formation of short rods (average diameter of 27 nm and length of 196 nm) and spheres (average diameter of 61 nm) in almost equal proportions. Further increase in treatment temperature to 900 °C (Figure 2d) resulted in the formation of large polygonal rods with diameter range of 78−150 nm and average length of 550 nm. The formation of polygonal rods possibly occurs through the cutting of the long nanotubes into short rods or wires which then bundle up into thicker and shorter rods than the original nanotubes. Based on the forgoing results it is clear that TNTs prepared by aHS undergo morphological transformation from tubes through nanowires to polygonal rods with temperature elevation. Subsequently, this transformation leads to a decrease in aspect ratio, which is indicative of particle growth in all dimensions.

For the μHS processed samples (Figure 2b), the materials remained tubular with size range of 8−11 nm in diameter. Though the diameter became bigger via Ostwald ripening process, after sintering at 700 °C the material transformed from tubular structure to form nanowires with length in micrometer region. At 700 °C the surfaces of nanowires became smoother because of the progress of surface diffusion. The formation of

nanowires with high aspect ratio suggests that the structure of material prepared μHS is thermally more stable than the aHS counterparts. This is also in agreement with a dramatic reduction in surface area. It is noteworthy that after sintering at 900 °C, the material's morphology dramatically transformed from nanowire to rod-like with significant reduction in aspect ratio due to particle growth. The material structural and morphological stability are largely influenced by method of preparation. Dimensions of tubes (length and diameter) are reproducible and are independent of method of preparation. Both aHS and μHS processes yielded tubes with similar dimensions. However, the mechanisms of formation seem to be different for the two methods.

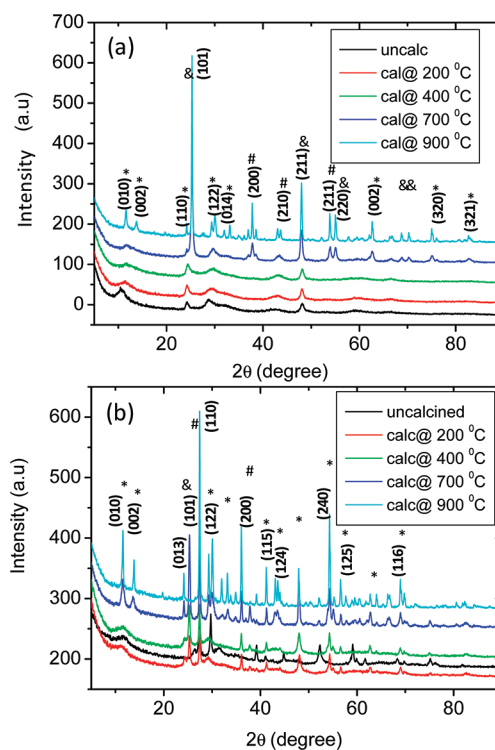Figure 3 shows the XRD profiles of hydrothermally synthesized material using aHS and μHS and sintered at

Figure 3. (a) XRD patterns of aHS-synthesized material sintered at different temperatures for 3 h. (b) XRD patterns of μHS synthesized material sintered at different temperatures for 3 h. In both figures, the symbol (*) refers to Ti_4O_7, (#) to TiO_2 anatase and (&) to TiO_2 rutile.

various temperatures for 3 h. At 200 and 400 °C, only a few broad peaks were observed, which could not be indexed to any known structure. However, previous studies have suggested that the broad peaks correspond to a titanate structure, $KTiO_2(OH)$[23] with a layered wall structure of titanate. The broadening is due to size effect. No other phase was present in the material. Figure 4 revealed that patterns are more or less similar up to 400 °C but the intensity of the diffraction peak at $2\theta \approx 10°$ was decreased and shifted to higher 2θ value because of a decrease in the interlayer distance for this plane. This contraction phenomenon of layers is probably due to the release of water molecules adsorbed and present in the spacing.

Furthermore, autoclave synthesized sample showed the presence of rutile phase with increased intensity and the evolution of new peaks at 700 °C. At higher temperatures (900
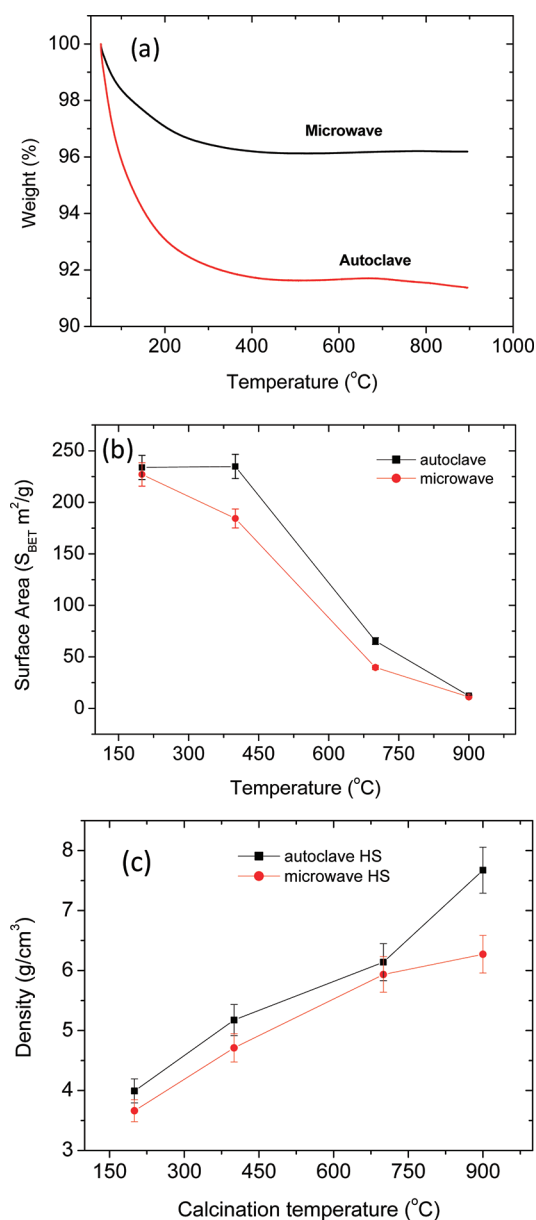
Figure 4. (a) Stability study through TGA profiles of the as prepared MW (μHS) and autoclave synthesized material (aHS) (b) surface area, (c) density of the aHS and μHS processed samples as a function of calcination temperature.

°C), the difference in rutile content is more clearly visible. It can be seen that with increasing sintering temperature, the peak intensities increased, whereas the peak widths became narrower because of coarsening of tubes. Moreover, more new intense peaks suggesting polyscrystalline material were observed at 900 °C, and these were indexed to a potassium hexatitanate ($K_2Ti_6O_{13}$) crystalline structure. This shows that the phase transformation of aHS-synthesized tubular structures occurs in two stages, i.e., first is the formation of rutile phase (TiO_2) from amorphous $KTiO_2(OH)$ followed by the formation of $K_2Ti_6O_{13}$ phase in the presence of TiO_2 (rutile). It is clear that the two titanate forms coexist with the rutile phase at elevated temperatures (700 −900 °C). It is also clear that the formation of $K_2Ti_6O_{13}$ is accelerated or influenced by the rutile phase. The intercalation of K ions into the structural framework of TiO_2 is a thermodynamically controlled phenomenon. The

surface free energy and surface stress play a pivotal role in the thermodynamic phase stability, which is a function of particle size. It is generally acceptable that transition from hydrous titania to TiO_2 can be attained by calcination at temperatures as low as 350 °C.[24] However, particles in this process tend to form aggregates and agglomerates.

Figure 3 shows the XRD patterns of material prepared by μHS and sintered at different temperatures. At low temperature (200 °C), the material comprises almost equal proportions of anatase and rutile phases as well a trace amounts of a titanate structure, Ti_4O_7. When the temperature was raised to 400 °C both anatase and rutile peak intensity increased whereas the Ti_4O_7 peaks became more prominent. At 700 °C more peaks emerged and could be indexed to rutile and titanate (Ti_4O_7) phases with very little anatase phase. It is noteworthy that as the sintering temperature was further elevated to 900 °C the anatase feature disappeared completely. The anatase phase is completely transformed to rutile and subsequently to a titanate structure (Ti_4O_7). It is well-known that rutile phase is more suitable than anatase phase for titanate phase formation and stability of the structure.[25] The presence of TiO_2 (anatase and rutile) and Ti_4O_7 structures show that potassium ions do not form part of the structural framework. The absence of K ions in the microwave product (Figures 1c and 1d) may have kinetic reasons. It is evident that the intercalation of K ions is as a result of longer reaction or processing times. On the basis of the foregoing results, it is clear that the structural composition of the TiO_2 based nanotubes can be controlled by varying the method of synthesis. However, phase transformation is independent of method of synthesis.

The phase transformation and phase transformation temperatures for samples prepared by aHS and μHS are different. Because both samples showed similar size and size distribution the difference in phase transformation temperatures could be attributed to structural difference and variance in the surface of tubes resulting from preparation method and conditions. The surface structure/surface energy has a significant influence on the overall nanotube stability, where a large fraction of atoms is at the surface.

The surface area results as determined from BET measurements as well as density of the samples are given in Table 1. These results show that as the sintering temperature is increased, the nanomaterials from both types of processing

Table 1. Properties of Powders Produced by Hydrothermal Process Using Conventional Heating and Microwave Irradiation All Sintered at Various Temperatures and Physical Properties of Microwave and Conventional Heating Synthesized TiO_2 Based Nanotubes Sintered at Various Temperatures

method of synthesis[a]	calcination temperature (°C)	S_{BET} (m^2/g)	density (g/cm^3)
aHS	200	233.9 ± 12.3	4.0 ± 0.06
aHS	400	234.8 ± 12.5	5.2 ± 0.08
aHS	700	65.4 ± 3.7	6.1 ± 0.09
aHS	900	12.3 ± 0.6	7.7 ± 0.10
μHS	200	227.1 ± 11.3	3.7 ± 0.05
μHS	400	184.4 ± 10.1	4.7 ± 0.07
μHS	700	39.7 ± 8.2	5.9 ± 0.09
μHS	900	11.1 ± 0.5	6.3 ± 0.09

[a]aHS = Conventional autoclave heating hydrothermal synthesis; μHS = microwave-assiated hydrothermal synthesis.
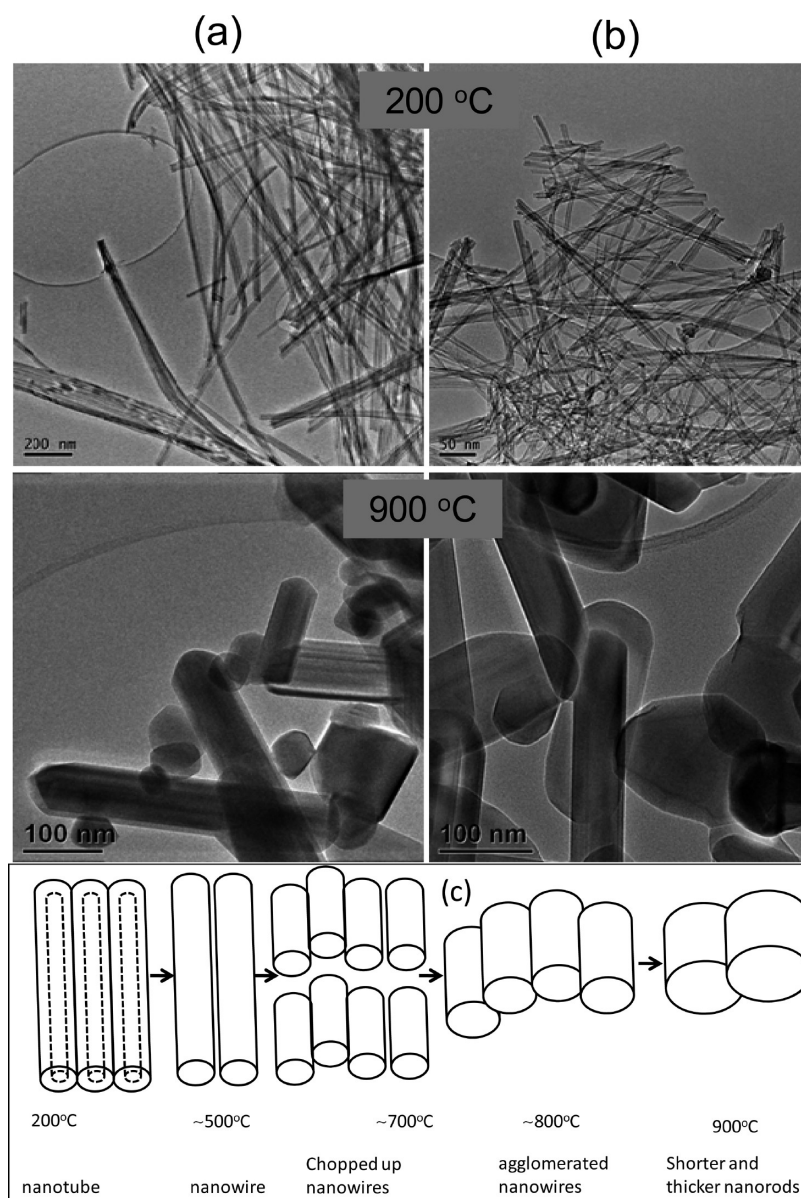
Figure 5. HRTEM images of (a) autoclave nanotubes sintered at 200 °C, (b) microwave nanotubes sintered at 200 °C, autoclave nanorods sintered at 900 °C, and microwave nanorods sintered at 900 °C, all for 3 h. (c) Proposed mechanism of transformation of nanotubes through nanowires to nanorods by thermal calcinations.

lose their surface areas but become denser. We also notice that autoclave-processed samples have, within experimental errors, slightly higher surface areas and higher densities across all sintering temperatures, as also displayed in Figure 1c.

The TGA results (Figure 4a) show a significant difference in weight losses of two typical samples process by autoclave and microwave HS respectively. A total weight loss of about 9% is observed for the conventionally prepared sample (autoclave). The first step of heating, from room temperature to 200 °C (∼6% weight loss) is attributed to evaporation of water adsorbed on the surface of the material. Further weight loss (∼3% total weight loss) in the temperature range of 200−400 °C is ascribed to the decomposition of structural hydroxide bound to the particle. However, microwave sample shows only ∼3% weight loss starting from room temperature to 200 °C. This weight loss is due to the loss of moisture absorbed on the surface of material. This finding is in agreement with the structural differences of the two samples (autoclave and

microwave). The difference in weight losses of the two samples is mainly due to the fact that the autoclave sample contains structural OH group, which can be removed only at temperatures above 200 °C. This clearly suggests that at temperatures above 200 °C, for conventionally prepared samples, the morphological changes and a dramatic increase in material density are due to contraction as a result of dehydration of interlayered OH group during the annealing process. It is also clear that the intercalation of potassium ions into the structural framework of TiO_2 influences the presence of OH group. In summary, microwave-processed samples display better temperature stability than autoclave counterparts.

Table 1 shows the surface area and density measurements of the powders sintered at various temperatures. Surface areas decrease as the calcination temperatures are increased while densities increase. This phenomenon is ascribed to grain growth but could also be influenced by the phase and structural composition. In both cases, critical density could not be
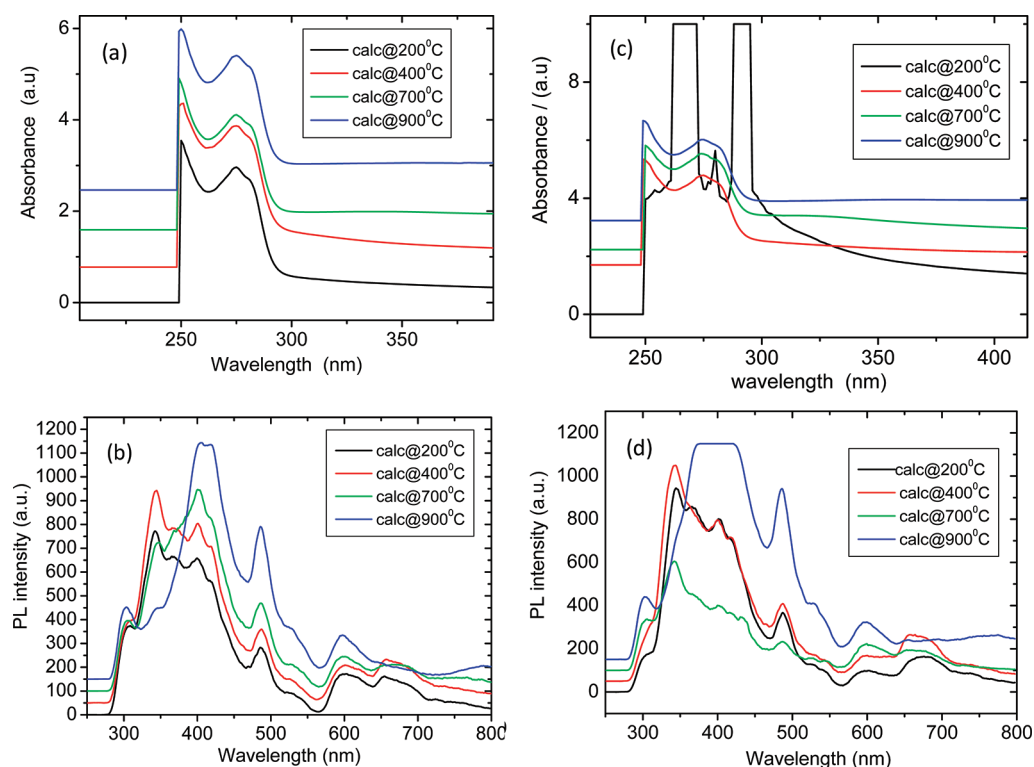
1660

dx.doi.org/10.1021/am2018089 | *ACS Appl. Mater. Interfaces* 2012, 4, 1656−1665

Figure 6. Absorbance for (a) microwave-processed and (c) autoclave-processed TiO$_2$ nanostuctures and (b, d) their corresponding photoluminescence properties, respectively.

reached, showing that the two materials could be denser with temperature elevation. Furthermore, the surface areas and densities of the powders prepared by autoclave were always higher than those produced by microwave. This is clearly shown by the plots b and c in Figure 4.

Figure 5 shows HRTEM of the two samples (autoclave and microwave) sintered at 200 and 900 °C. At low temperature (200 °C), both samples (aHS and μHS) retained a tubular structure (Figures 5a, b). It is interesting to note that the rods formed at high temperatures for both samples have a polycrystalline structure. This explains the wide size distribution after sintering at high temperature. It is believed that nanocrystals attach to each other from grain boundaries such that the overall structure grows into a rodlike structure by a self-assembly process.

3.2. Comparison. The results have shown the advantages of microwave irradiation during hydrothermal synthesis of powders. Microwave irradiation delivers energy directly to the reaction media thereby shortening both the heating and cooling times. This prevents uncontrollable heating of the thick walls of high pressure reaction vessels like in the case of autoclave. Conventional systems (i.e., autoclave) have high thermal inertia, whereas temperature control is also more difficult to maintain than in the case of low inertia systems. The use of microwave as heating method during hydrothermal process allowed for a more precise control of process parameters such as time, pressure, power, and temperature while ensuring high purity (phase) of the product. The precision of the microwave system allowed for a good study of the effects of synthesis conditions on the phase composition and grain size distribution of the powder. Although the same was done for the autoclave sample, structural composition could not be controlled.

It is understood that the tubes prepared by conventionally heated hydrothermal synthesis have a layered structure with potassium ions (K$^+$) intercalated and affecting the overall crystallinity and stability of the tubes. It is for this reason that conventionally prepared tubes showed less stability than those prepared by microwave assisted HT process. It is therefore believed that the removal of these intercalated ions (K$^+$) would essentially improve the stability and this could be achieved by acid treatment of the precipitate after HT treatment.

3.2.1. Mechanism of Phase Transformation—Conventional Heating. It is believed that the disintegration of a titanate, KTiO$_2$(OH), upon various sintering stages (400−900 °C) led to contraction and breaking ascribed to dehydration phenomenon. This supports the fact that phase transformation of nanostructural phase of sample prepared by microwave synthesis occurs only at relatively higher temperatures because the material is anhydrous.[26−30]

After annealing at 700−900 °C, the initial form of titanate structure, KTiO$_2$(OH), disappeared while the tubular structure also disappeared. The evolution of rods with different dimension is observed. This shows the deterioration of layered structure and the collapse of walls of this titanate structure (Figure 2). The degradation of layered structure and the evolution of rutile phase at elevated temperature are well-reported phenomena.[6,31] The reason for this phase transformation is correlated to the dehydration of interlayered OH group during annealing process.

Our findings show disparity from the literature. M. Qamar et al.[32] reported that the tubular structures transform completely to irregular spherical particles at 900 °C. However, our results show that at 900 °C both microwave and conventionally synthesized samples contained a rodlike structure (Figure 5). The disparity is attributed to difference in material stability
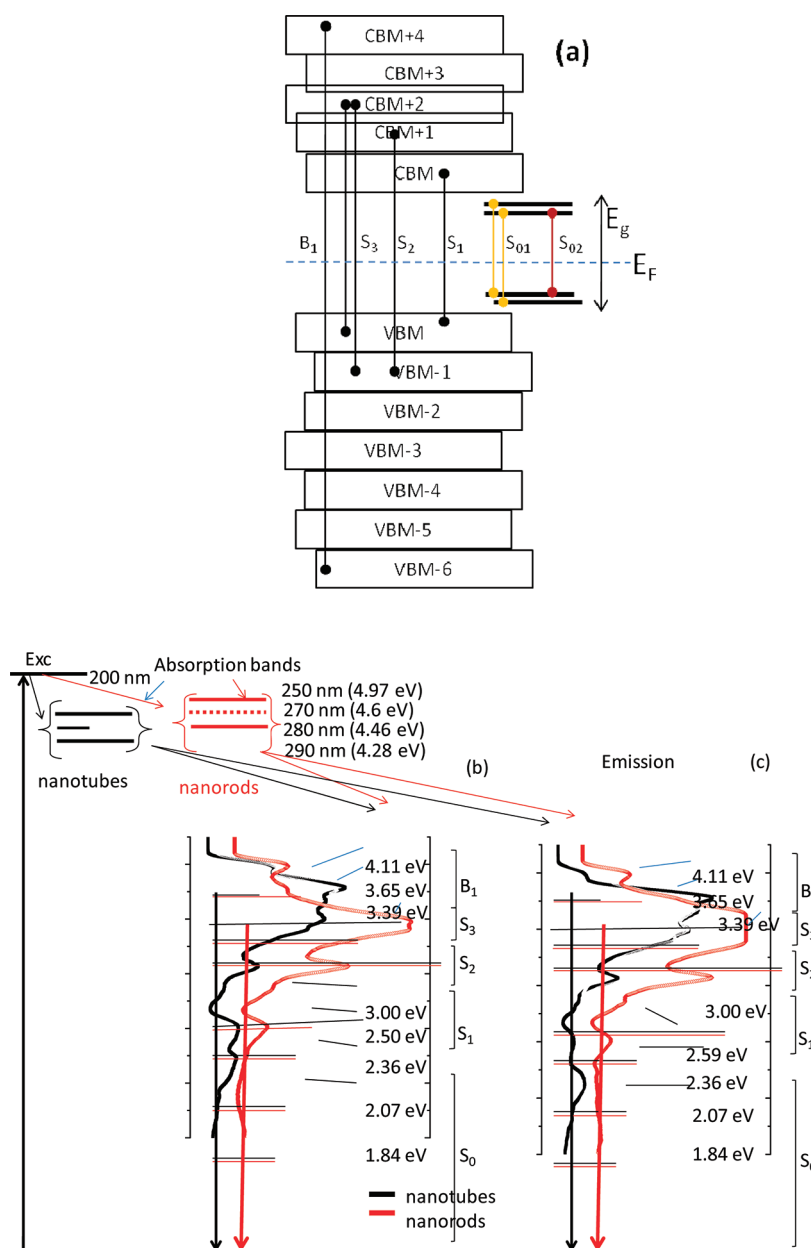
Figure 7. (a) Schematic representation of the PL spectra in the form of energy diagrams for (a) TiO$_2$ system as adapted from Georgi et al.[36] CBM represents the mth sub-band in the conduction band and similarly VBM the mth sub-band level in the valence band. (b) PL spectra in form of band energy diagrams for microwave-derived TiO$_2$ nanotubes and nanorods, and (c) autoclave-derived TiO$_2$ nanotubes and nanorods.

which is largely influenced by method of preparation.[32] M. Qamar et al. demonstrated that the quantity of metal ions present in the sample plays an important role in the stability and phase transformation of the nanotubes.[32] In this study, we have shown that we could control the presence of metal ions (K$^+$) by varying the synthesis method and conditions. We have also shown that phase transformation of TiO$_2$ derived nanotubes free of metal ions and containing metal ions occurs via different pathways. It must be noted that prior to heating nanotubes tended to form a combination of bundles and free nanotubes. However, after heating at high temperatures (700 °C) nanotubes changed to thick nanorods or one dimensionally connected nanoparticles.

3.2.2. Mechanism of Phase Transformation—Microwave Synthesis. Studies have shown that there are various factors that influence the phase transformation of anatase to rutile and

subsequently to a titanate phase. These include temperature, pressure, particle size, additive/dopant, and hydrothermal conditions used.[33] The transition from anatase to rutile reaches completion at about 800 °C, whereas a complete transformation to a titanate form of TiO$_2$ (i.e., Ti$_4$O$_7$) occurs at temperature of about 1200 °C for P25 Degussa TiO$_2$ with spherical morphology.[34,35] The microwave synthesized sample showed the presence of a titanate phase at 700 °C indicating that the phase transition temperature was decreased. The decrease in temperature may be due to size effects in the nanoscaled materials. This is supported by the numerous observations that indicate the decrease in melting temperatures in nanomaterials. The transition to a titanate phase occurs via the formation of a metastable phase as an intermediate product. Size effects are believed to play a pivotal role in the phase transformation and suppression of transformation temperature.

Table 2. Summary of the PL Properties of TiO₂ Nanorods and Nanorods

surface reconstruction	Georgi et al.[36]		present PL energies		remarks
			microwave synthesized	autoclave synthesized	
(1 × 1) reconstruction or nanotubes	B₁	3.9 eV	302 nm (4.11 eV)	320 nm	built up mixing transitions (at some *k* points near the Γ, along the Γ−J, and Γ−K directions) from a few bands below (from VBM-6 to VBM) to a few bands above (from CBM to CBM+4) the Fermi level
	S₃	3.2 eV	366 nm (3.39 eV)	366 nm	originate from the mixing of the independent quasi-particle (IQP) transition at the Γ point from VBM and VBM-1, as in S1, to the first three unoccupied bands (CBM to CBM+2)
	S₂		415 nm		originate from the mixing of the independent quasi-particle (IQP) transition at the Γ point from VBM and VBM-1, as in S1, to the first three unoccupied bands (CBM to CBM+2)
	S₁	3.2 eV	485 nm		originates from the mixing vertical transitions at Γ, from the two highest occupied valence bands (VBM, CBM+1) that are located mainly on the Ti atoms, with d_{xy} orbital characters
	S₀		525 nm (2.36 eV)		possibly originate from excitons trapped at impurities and defects such as at Ti−- K or O−K sites.
			600 nm (2.07 eV)		
			675 nm (1.84 eV)		
(1 × 4) reconstruction or nanorods	B₁′	3.9 eV	302 nm (4.11 eV)	302 nm	same as in B₁
	S₃′		366 nm (3.39 eV)	366 nm	same as in S₃
	S₂′		400 nm		same as in S₂
	S₁′	3.5 eV	480 nm (3.00 eV)		same as in S₁
	S₀		525 nm (2.36 eV)		possibly originate from excitons trapped at impurities and defects such as at Ti− K or O−K sites.
			600 nm (2.07 eV)		
			675 nm (1.84 eV)		

This is probably because of the fact that the tubular structures might have a higher structural energy than spherical counterparts because of increased surface free energy, which reduces the energy required to reach the activated state.

It is clear that the intercalation of K ions into the structural framework of TiO₂ is dependent on the time and temperature of processing. Though we have two products with more or less similar specifications, the autoclave sample is a thermodynamically favored product, whereas the microwave is kinetically favored. The stability of the product is by and large influenced by this.

3.3. UV−Vis−IR Absorption and Photoluminescence Spectra. Well-resolved photoabsorption and PL results are shown in Figure 6. Absorption in the autoclave samples shows a drastic blue shift from those calcined below 200 °C to those calcined at more than 200 °C. The samples calcined below 200 °C display absorption peaks at wavelengths of 270, 280, and 290 nm whereas those calcined above 200 °C show peaks at wavelengths of 260 and 280 nm. In the former case, the absorption peaks are sharp and the 270 and 290 nm peaks are higher than the saturation limit of the detector. In the latter case, the peaks are broadened. It must be noted that the 260 nm peaks are on the instrument cutoff limit and therefore part of the 260 nm absorption peaks are cut off.

The PL results suggest that for both autoclave and microwave-processed samples, the effects of calcination are observed only at temperatures above 700 °C (the nanotube-to-nanorod transformation temperature) when the emission peaks at 302, 340, 400, 480, 575, 600, and 675 nm now appear with 340 nm peak absent. The profiles for both autoclave-processed and microwave-processed samples are quite similar. It must be noted that, for microwave-processed materials, the peak at 400 nm is sharper, red-shifted to 415 nm, and unsaturated, whereas

the same is broad at 400 nm and saturated for autoclave samples. This may suggest that the autoclave samples have higher quantum efficiency for this peak than the microwave samples. It was also noted that the 480 nm peaks in the microwave samples are red-shifted to about 485 nm. The red-shifts in the microwave-processed materials may suggest that the crystallite sizes in microwave-processed materials are slightly larger in these samples than the autoclave-processed materials, although the particle sizes compare in reverse.

To explain the well-resolved PL spectra of the present TiO₂ samples, we based our diagrams on those of Giorgi et al.'s ab initio assignment (Figure 7a) of the TiO₂ dielectric properties.[36] First the terms used here are defined: *k* is the exciting photons' wave vector relative to the sample crystallite;, Γ, J, and K are the labels for first, second and third Brillouin zones of the wave vector for the excited or vibrating crystallite upon interaction of the exciting photons with the TiO₂ crystallite; the VBM-n and CBM-n are, respectively, M-n-stratified valence bands and conduction band of the TiO₂ electronic structure.

The peak at 302 nm (4.11 eV) is herein assigned to a bulk exciton, labeled B₁, which migrates to the surface upon excitation. This is built up by mixing transitions (at some *k* points near the Γ, along the Γ−J and Γ−K directions) from a few bands below (from VBM-6 to VBM) to a few bands above (from CBM to CBM+4) the Fermi level. The peak at 340 nm (3.65 eV) labeled S₃ and that at 400 nm labeled S₂ are known to originate from the mixing of the independent quasi-particle (IQP) transition at the Γ point from VBM and VBM-1 to the first three unoccupied bands (CBM to CBM+2). The feature labeled S₁, like S₂ and S₃, originates from the mixing vertical transitions at Γ, from the two highest occupied valence bands (VBM, CBM+1) that are located mainly on the Ti atoms, with d_{xy} orbital characters (from the figures, the broadening of

1663

dx.doi.org/10.1021/am2018089 | *ACS Appl. Mater. Interfaces* 2012, 4, 1656−1665

autoclave 400 nm peak and the red-shifts). These results are compared with our present work and are summarized in Table 2.

We have also redrawn both the absorption and PL results into a proposed energy diagram in panels b and c in Figures 7 for microwave-processed and autoclave-processed materials, respectively. In both figures, an excitation energy from 200 nm (5.5 eV) photons leads to varying absorption from 260 nm (4.8 eV) to 290 nm (4.28 eV) in the two sets of samples. After absorption, the samples emit photons of energies ranging from 302 nm (4.11 eV) to 675 nm (1.84 eV). Because we have observed drastic change in PL in samples calcined above 700 °C, we have represented these samples in red and those calcined below 700 °C as black. From recent ab initio calculations on the optical properties of TiO_2,[36] it was reported that not all the crystal planes of the anatase are important in the photocatalytic properties of anatase. Only the (001) plane presents enhanced catalysis and optical properties. When such a plane is cleaved, the as-cleaved surface has surface construction of (1×1), whereas the reconstructed (001) planes has a surface reconstruction of (1×4). It was reported that the as-cleaved (1×1) has better photocatalytic properties than the (1×4) surface. Also, although many experimental reports[36−38] on the PL of TiO_2 have assigned only the broad unresolved Lorentzian-shaped spectra to surface-trapped excitons, the recent ab initio report has observed a finer structure of the (001) (1×1) and (001) (1×4) TiO_2 surfaces.

Because of high resolution in our PL measurement system, however, in our present samples, we observed extra PL features at 525 nm (2.36 eV), 600 nm (2.07 eV), and 675 nm (1.84 eV) not yet observed even in the ab initio reports. We have labeled these features herein as S_0 in keeping with the order set by Georgi et al.[36] We suspect these to originate from excitons trapped at impurities and defects such as at Ti−K or O−K sites.

In summary, nanorods tend to absorb higher energy photons than nanotubes but emit lower energy photons than nanotubes. This property displayed by nanorods can be useful in selective solar absorbers.

3.4. H_2-Sensing Properties of Nanorods and Nanotubes of TiO_2.

After showing that autoclave samples have slightly higher surface area than those processed by microwaves, H_2 gas-sensing experiments on autoclave samples were commenced. For convenience only two samples made by autoclave hydrothermal synthesis were compared here: a sample containing nanotubes (calcined at 200 °C) and another sample containing nanorods (calcined at 900 °C). The interest was to first check the shape effect (i.e., nanotube or nanorod) rather than the process of synthesis after seeing from PL above that it has smaller influence on emission than the shape of the materials has.

The H_2 gas-sensing properties (S, $\tau_{response}$, $\tau_{recovery}$) are obtained from resistance transient curves illustrated in panels a and b in Figure 8. Here, S is the sensitivity of the sample to H_2 gas exposure defined as $S = |R_{in} - R_{out}|/R_{out}$, the fractional change in resistance between absence (R_{out}) and presence (R_{in}) of the analyte gas. The times $\tau_{response}$ and $\tau_{recovery}$ are response and recovery times, respectively, defined as the time taken for the resistance to change by 90% of the initial value during the gas-in cycle and gas-out cycle, respectively.

Figure 8a shows a typical resistance−time curve for nanorods and nanotubes. It can, thus, be seen that there is a greater change in resistance for nanotubes when the samples are in absence and presence of H_2 gas, hence higher S (0.976) for
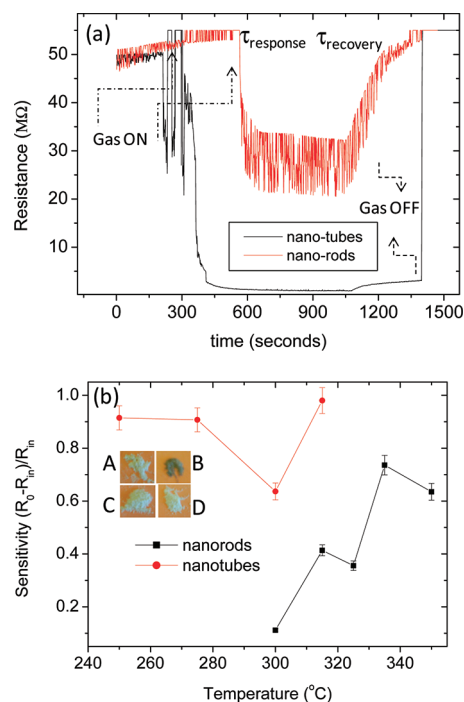

Figure 8. (a) Resistance-time profiles for TiO_2 nanotubes and nanorods showing much higher changes in resistance in the nanotubes than in the nanorods, comparable response times but faster recovery from tubes than from rods. (b) Sensitivity of nanotubes and nanorods at various temperatures. Tubes have higher sensitivity at lower working temperatures than nanorods. (c) Photographs of samples before and after sensing experiments: A and B are nanorods before and after H_2 sensing and C and D are nanotubes before and after H_2 sensing experiments.

tubes than for rods (0.400). This could be due to the higher surface area. Also although the response times are twice as long for tubes (∼20 s for tubes and ∼10 s for rods), the recovery time for tubes is much shorter (∼5 s) than that for nanorods (∼120 s). Thus nantoubes sense H_2 faster and recover faster than nanorods.

Nanotubes have a lower threshold temperature (250 °C) for H_2 gas sensing than the nanorods (300 °C). Figure 8b clearly shows that the TiO_2 nanotubes not only show consistently higher sensitivity to H_2 at all temperatures than in its nanorod form but also require lower threshold temperatures (250 °C) than the nanorods do (300 °C).

Figure 8c shows photographs of autoclave samples that were used for H_2 gas sensing measurements. A and B are photographs for nanorods before and after H_2 sensing; respectively, whereas C and D are for nanotubes before and after H_2 gas sensing, respectively. There is a clear evidence of color change in the nanorods after H_2 gas sensing that is not observed in the nanotubes. This may mean that tubes do not engage in serious chemical reaction with H_2 gas molecules as do the rods (i.e., H_2 weakly adsorbed on the surface of the tubes). This may lead to nonstoichiometric or suboxide material in the rods. Another possibility is that H_2 gas serves as a source of protons that when injected in the TiO_2 matrix may lead to an irreversible electrochromic behavior in the rods.

4. CONCLUSIONS

Although recent studies have highlighted the confusion around the structure of TiO_2-derived nanotubes, here we demonstrated

that the nature of heating determines the structure of the final tubular product. K$^+$-free titanate tubes, wires and rods were prepared by microwave-assisted hydrothermal process including thermal post-treatment steps in the absence of acid treatment.

The surface structure of TiO$_2$ derived nanotubes prepared by hydrothermal synthesis is influenced by the nature of heating applied (i.e., conventional and microwave heating). Tubes prepared by conventional method of heating showed relatively lower thermal stability when compared to those prepared by microwave irradiation. The structural composition also varied. Microwave synthesis produced phase pure TiO$_2$ nanomaterials comprising anatase and rutile. Upon sintering at 900 °C a phase transition occurs resulting in the formation of a titanate structure without potassium in the structural framework (Ti$_4$O$_7$). The transition was accompanied by morphological transformation from tubular structures to nanowires and subsequently to rod-like shape. However, conventional HT synthesis yielded a titanate tubular structure, KTiO$_2$(OH), that transformed to a rod like titanate and then again to short-rod morphology with a different titanate form (K$_2$Ti$_6$O$_{13}$).

Microwave-synthesized samples were found to be more polyscrystalline than conventionally produced (autoclave) materials at all sintering temperatures.

However, autoclave samples showed higher PL intensities than the microwave ones. Microwave samples showed red-shifts especially in the 400 and 480 nm PL peaks, showing the tube could be slightly larger here than in the autoclave samples. In both cases, calcinations temperature shows a drastic change in the PL spectra with the disappearance of the 340 nm peak and the enhancement of the 400 nm. We also have found new features in the PL spectra at 525 nm (2.36 eV), 600 nm (2.07 eV), and 675 nm (1.84 eV) not yet observed even in the ab initio reports.

Nanotubes tend to show higher sensitivity to H$_2$ gas exposure than nanorods possibly due to higher surface area in tubes than rods. Tubes can be twice as slow in response as the rods but the recovery time for nanotubes is much shorter (60 times more) than that for the nanorods, which may be an indication of weaker adsorption of H$_2$ on the nanotubes than on the nanorod surface, as also seen in the color change in the nanorods.

■ AUTHOR INFORMATION

Corresponding Author

*E-mail: LSikhwivhilu@csir.co.za (L.M.S.); bmwakikunga@csir.co.za (B.W.M.); rsuprakas@csir.co.za (S.S.R.).

Notes

The authors declare no competing financial interest.

■ ACKNOWLEDGMENTS

■ REFERENCES

(1) Amano, F.; Yasumoto, T.; Shibayama, T.; Uchida, S.; Ohtani, B. Appl. Catal., B **2009**, 89, 583.
(2) Suzuki, Y.; Pichon, B. P.; D'elia, D.; Beauger, C.; Yoshikawa, S. J. Ceram. Soc. Jpn. **2009**, 117, 381.
(3) Yu, H. G.; Yu, J. G.; Cheng, B.; Zhou, M. H. J. Solid State Chem. **2006**, 179, 349.
(4) Nian, J.-N.; Teng, H. J. Phys. Chem. B **2006**, 110, 4193.
(5) Lan, Y.; Gao, X. P.; Zhu, H. Y.; Zheng, Z. F.; Yan, T. Y.; Wu, F.; Ringer, S. P.; Song, D. Adv. Funct. Mater. **2005**, 15, 1310.
(6) Yoshida, R.; Suzuki, Y.; Yoshikawa, S. J. Solid State Chem. **2005**, 178, 2179.
(7) Fujishima, A.; Honda, K. Nature **1972**, 238, 37.
(8) Dagan, G.; Tomkiewicz, M. J. Phys. Chem. **1993**, 97, 12651.
(9) Fukushima, K.; Yamada, I. J. Appl. Phys. **1989**, 65, 619.
(10) Bavykin, D. V.; Milsom, E. V.; Marken, F.; Kim, D. H.; Marsh, D. H.; Riley, D. J.; Walsh, F. C.; El-Abiary, K. H.; Lapkin, A. A. Electrochem. Commun. **2005**, 7, 1050.
(11) Hou, L. R.; Yuan, C. Z.; Peng, Y. J. Hazard. Mater. **2007**, 139, 310.
(12) Xu, J. C.; Lu, M.; Guo, X. Y.; Li, H. L. J. Mol. Catal. A **2005**, 226, 123.
(13) Bavykin, D. V.; Friedrich, J. M.; Walsh, F. C. Adv. Mater. **2006**, 18, 2807.
(14) Grätzel, M.; O'Regan, B. J. Photochem. Photobiol. **1991**, 353, 737.
(15) Alam Khan, M.; Shaheer Akhtar, M.; Woo, S. I.; Yang, O.-B. Catal. Commun. **2008**, 10, 1.
(16) Chopra, N. G.; Luyken, R. J.; Cherry, K.; Crespi, V. H.; Cohen, M. L.; Louie, S. G. Science **1995**, 269, 966.
(17) Satishkumar, B. C.; Govindaraj, A.; Voli, E. M.; Basumallic, L.; Rao, C. N. R. J. Mater. Res. **1997**, 12, 604.
(18) Nakamura, H.; Matsui, Y. J. Am. Chem. Soc. **1995**, 117, 2651.
(19) Ajayan, P. M.; Stephan, O.; Redlich, P.; Colliex, C. Nature **1995**, 395, 564.
(20) Hoyer, P. Langmuir **1996**, 12, 1141.
(21) Bavykin, D. V.; Gordeev, S. N.; Moskalenko, A. V.; Lapkin, A. A.; Walsh, F. C. J. Phys.Chem. B **2005**, 109, 8565.
(22) Masaki, N.; Uchida, S.; Yamane, H.; Sato, T. Chem. Mater. **2002**, 14, 419.
(23) Sun, X.; Chen, X.; Li, Y. Inorg. Chem. **2002**, 41, 4996.
(24) Erdey, L.Gravimetric Analysis; Pergamon: New York, 1965, 459.
(25) Feist, T. P.; Davies, P. K. J. Solid State Chem. **1992**, 101, 275.
(26) Kasuga, T.; Hiramatsu, M.; Hoson, A.; Sekino, T.; Niihara, K. Langmuir **1998**, 14, 3160.
(27) Sun, X.; Li, Y. Chem.—Eur. J. **2003**, 9, 2229.
(28) Yao, B. D.; Chan, Y. F.; Zhang, X. Y.; Zhang, W. F.; Yang, Z. Y.; Wang, N. Appl. Phys. Lett. **2003**, 82, 281.
(29) Zhang, S.; Li, W.; Jin, Z.; Yang, J.; Zhang, J.; Du, Z.; Zhang, Z. J. Solid State Chem. **2004**, 177, 1365.
(30) Kim, G. S.; Godbole, V. P.; Seo, H. K.; Kim, Y. S.; Shin, H. S. Electrochem. Commun. **2006**, 8, 471.
(31) Poudel, B.; Wang, W. Z.; Dames, C.; Huang, J. Y.; Kunwar, S.; Wang, D. Z.; Banerjee, D.; Chen, G.; Ren, Z. F. Nanotechnology **2005**, 16, 1935.
(32) Qamar, M.; Yoon, C. R.; Oh, H. J.; Kim, D. H.; Jho, J. H.; Lee, K. S.; Lee, W. J.; Lee, H. G.; Kim, S. J. Nanotechnology **2006**, 17, 5922.
(33) Banfield, J. F.; Bischof, B. L.; Anderson, M. A. Chem. Geo. **1993**, 110, 211.
(34) Sikhwivhilu, L. M. PhD thesis, University of the Witwatersrand, Johanessburg, South Africa, 2007; p 189.
(35) Mwakikunga, B. W.; Sideras-Haddad, E.; Witcomb, M.; Arendse, C.; Forbes, A. J. Nanosci. Nanotechnol. **2009**, 9, 3286.
(36) Giorgi, G.; Palummo, M.; Chiodo, L.; Yamashita, K. Phys. Rev. B **2001**, 84, 073404−1−07340.
(37) Liu, B.; Wen, L.; Zhao, X. Mater. Chem. Phys. **2001**, 106, 350.
(38) Xiang, Q. J.; Lv, K. L.; Yu, J. G. J. Appl. Catal. B **2010**, 96, 557.

1665

dx.doi.org/10.1021/am2018089 | ACS Appl. Mater. Interfaces 2012, 4, 1656−1665